



CrossMark
click for updates

Cite this: *RSC Adv.*, 2015, 5, 24056

Novel hybrid Sr-doped TiO₂/magnetic Ni_{0.6}Zn_{0.4}Fe₂O₄ for enhanced separation and photodegradation of organics under visible light

Fuming Liu,^a Yu Xie,^{*a} Changlin Yu,^c Xiaoming Liu,^a Yuhua Dai,^a Lianjun Liu^{*b} and Yun Ling^a

Titanium dioxide (TiO₂) has been intensively used as a photocatalyst for the degradation of organic pollutants in water, but is typically obstacle by a low efficiency, costly separation, limited visible light response, and poor recyclability. Herein, we provided a reliable method to simultaneously tackle these four obstacles by developing an integrated and multifunctional hybrid photocatalyst/magnetic material, *i.e.*, Sr-TiO₂/Ni_{0.6}Zn_{0.4}Fe₂O₄. This novel hybrid not only demonstrated a high efficiency (90–100%) and a good cycling performance (90% maintenance) for photodegradation of bisphenol A (BPA) under both UV and visible light irradiation, but it can also efficiently work at a wide pH range (4–10) and can be easily separated from water for reuse only by introducing an external magnetic field. The materials structure-to-activity correlation has also been investigated. It was found that doping Sr²⁺ and a coupling magnetic material with TiO₂ could extend the visible light response and create active defects in TiO₂, which were responsible for the nearly three times higher activity than that of commercial TiO₂(P25) under visible light. On the other hand, doping excessive Sr²⁺ lowered the surface area, enlarged the crystalline size and caused particle aggregation; thus, leading to a decrease in photocatalytic activity of the hybrid. These further modifications in the hybrid materials can provide a competitive alternative to control the organic pollutants in waste water.

Received 11th January 2015
Accepted 18th February 2015

DOI: 10.1039/c5ra00187k

www.rsc.org/advances

1. Introduction

Photodegradation of organic pollutants using photocatalysts (*e.g.*, ZnO, TiO₂, WO₃, CdS) holds a great promise to purify water and has been investigated intensively over the last decade.^{1–3} Among the photocatalysts, TiO₂ has received great interest because of its chemical stability, high photocorrosion resistance, non-toxicity, and low-cost.^{3–8} However, bare TiO₂ has a very low quantum efficiency primarily because of fast recombination rates of electron and hole pair (e⁻-h⁺) and limited visible light responses (due to its wide band gap in the range of 3.0–3.2 eV).^{1,8} The low efficiency of TiO₂ is a major barrier for commercializing this photocatalytic technology. Complicated separation of photocatalyst for regeneration and reuse may also impede its practical application, but this challenge is seldom addressed in the literature.^{9–11} Generally, a TiO₂-based power was suspended in a solution for the photodegradation of

organic pollutants, and it often required a filtration or centrifugation process to separate the photocatalyst from water. This process may increase the cost and brings a potential genotoxicity due to some residual organics adsorbed on the solids.^{2,12} Therefore, it is urgent and necessary to develop high performance and easily recycled TiO₂-based photocatalysts.

To improve the photocatalytic efficiency of TiO₂, great efforts have been made to modify TiO₂ either by incorporating noble metals (*e.g.*, Ag) or metal oxides (*e.g.*, Fe₂O₃) to act as electron traps and inhibit the recombination of e⁻-h⁺ pairs,^{2,8,13–16} or by doping nonmetals (*e.g.*, N) or co-doping with nonmetals and transition metal ions (*e.g.*, Cr³⁺, Cu²⁺, Co²⁺, Mg²⁺) to extend the visible light response.^{9,17–23} Alternatively, pure or modified perovskite strontium titanate (SrTiO₃) and SrTiO₃/TiO₂ heterojunctions have also been investigated as a candidate for the photodegradation of organic pollutants.^{23–27} However, a few studies have been conducted on Sr²⁺ doped TiO₂ for the photodegradation of organic compounds. Very recently, Li *et al.*²⁸ synthesized Sr²⁺-doped ZnO composites and attributed its enhanced performance over ZnO for RhB degradation under visible light to the narrowed band gap and the formation of active defects to trap electrons. Along this line, it is expected that doping Sr²⁺ into the TiO₂ lattice will lead to an enhanced photocatalytic degradation of bisphenol A (BPA).

^aDepartment of Materials Chemistry, Nanchang Hangkong University, Nanchang, Jiangxi Province, 330063, PR China. E-mail: xieyu_121@163.com; Fax: +86 791 83953373; Tel: +86 791 83953373

^bMechanical Engineering Department, University of Wisconsin–Milwaukee, Milwaukee, WI, 53211, USA. E-mail: liul@uwm.edu; Tel: +1 216 650 9842

^cSchool of Metallurgy and Chemical Engineering, Jiangxi University of Science and Technology, Ganzhou, Jiangxi Province, 341000, PR China



To overcome the obstacle of TiO₂ powder separation from solution, several efforts have been attempted to anchor TiO₂ on solid substrates (e.g., Ti mesh)^{4,11,29–33} or incorporate TiO₂ with magnetic materials (e.g., ferrite).^{34–40} Immobilizing TiO₂ on solid substrates is restricted to laboratory or small-scale applications because of the complicated preparation process, weak attachment of TiO₂ on the foreign substrates, and deficient immersion and dispersion of TiO₂ in the slurry solution. On the other hand, magnetic separation is a promising route to recover the used photocatalysts only by applying an external magnetic field. A number of studies have been attempted to fabricate core-shell structured magnetic material/photocatalysts for the photo-degradation of organics, including Fe/TiO₂/Ag, Fe/V/TiO₂, nickel ferrite/N-TiO₂, and strontium ferrite/N-TiO₂.^{9,34,37,40} Unfortunately, the nanosized core magnetic materials are easily oxidized (e.g., Fe₃O₄ oxidized to Fe₂O₃) or rapidly transform in the crystal phase (e.g., γ -Fe₂O₃ ferromagnetic to α -Fe₂O₃ paramagnetic) when the calcination temperature is over 400 °C.^{34,40} Obviously, it is still a challenge to produce the TiO₂-coated magnetic nanoparticles with concurrent good stability, high visible light activity and good magnetic properties.

To simultaneously overcome the challenges in the catalytic efficiency and separation of TiO₂-based photocatalysts, in this work, we designed a novel hybrid by integrating a photocatalyst with magnetic material, i.e., Sr-TiO₂/Ni_{0.6}Zn_{0.4}Fe₂O₄. We hypothesize that (1) doping TiO₂ with Sr²⁺ could create some active defects and promote visible light absorption, and thus enhancing the charge separation and extending visible light response, (2) introducing Zn into NiFe₂O₄ could prevent the phase transition and assure good magnetic properties,^{41,42} and using Ni_{0.6}Zn_{0.4}Fe₂O₄ as magnetic core not only harvests visible light but also facilitates photocatalyst separation, and (3) an interface may be formed between Sr²⁺-doped TiO₂ and magnetic Ni_{0.6}Zn_{0.4}Fe₂O₄, and thus inducing a synergistic effect to remove organics with an exceptional performance. To the best of our knowledge, for the first time this multifunctional material for water treatment has been developed. All the materials used (Ti, Sr, Ni, Zn, and Fe) to build the nanostructure are inexpensive and earth-abundant. The sol-gel method employed to prepare the hybrid is also simple and easy to scale-up. Another feature in this work is to evaluate the cycling performance of the hybrid photocatalyst/magnetic material under both UV and visible light irradiation, and attempt to establish the structure-to-activity relationships.

2. Materials and methods

2.1 Synthesis of magnetic Ni_{0.6}Zn_{0.4}Fe₂O₄ nanoparticles

Ni_{0.6}Zn_{0.4}Fe₂O₄ nanoparticles were prepared by a self-propagating combustion method. In brief, 0.1 mol nickel nitrate (Ni(NO₃)₂·6H₂O), 0.067 mol zinc nitrate (Zn(NO₃)₂·6H₂O) and 0.333 mol iron nitrate (Fe(NO₃)₃·9H₂O) were dispersed into 100 ml deionized water with vigorous stirring. Citric acid (0.5 mol) was then added into the solution, using ammonium hydroxide to adjust the pH around 10.0. Next, the solution was heated in a water bath at 70 °C by microwave irradiation until

the sol was formed. The as-received sol was finally dried in an oven at 100 °C for 24 h.

2.2 Synthesis of hybrid Sr-TiO₂/magnetic material

The hybrid Sr-TiO₂/magnetic materials were prepared by a sol-gel method. Typically, in a beaker A, 10 ml of tetrabutyl titanate (C₁₆H₃₆O₄Ti), 1 g of Ni_{0.6}Zn_{0.4}Fe₂O₄ nanoparticles, and 40 ml of absolute ethyl alcohol were uniformly mixed. In a beaker B, a certain amount of strontium nitrate (Sr(NO₃)₂) and starch (the mass ratio of Sr(NO₃)₂ to starch is 0.02 : 0.5, 0.05 : 1, 0.1 : 1.5, 0.2 : 2.5), 5 ml de-ionized water, and 15 ml acetic acid were mixed. The mixture was heated for 5 min by microwave irradiation to get a homogeneous solution. Next, the solution in the beaker B was added dropwise to beaker A with mechanical stirring for 2 h. The mixed solution was aged at 70 °C for 24 h. The obtained gel was then dried and calcined at 550 °C in air for 4 h. The final hybrid materials were denoted as Sr_xTi/M (M = Ni_{0.6}Zn_{0.4}Fe₂O₄), where *x* is the nominal weight percentage of Sr²⁺ (i.e., 0.1 wt%, 0.25 wt%, 0.5 wt%, and 1 wt%). For comparison, Ti/M and Sr_{0.25}Ti were also prepared using a same procedure as SrTi/M.

2.3 Characterization

The crystal structure of Sr-TiO₂/Ni_{0.6}Zn_{0.4}Fe₂O₄ materials were characterized by X-ray diffraction (XRD) using a Bruker D8 Advance X-ray diffractometer with monochromated high-intensity CuK α radiation ($\lambda = 0.15418 \text{ \AA}$) in the 2θ range of 10–80°. The morphology and particle size of the materials were identified by field emission scanning electron microscopy (FESEM). Transmission electron microscopy (TEM) (JEOL TEM-3010) was used to approach the lattice fringes operating at an accelerating voltage of 300 keV. The surface area and porosity of the as-synthesized materials were examined by N₂ adsorption/desorption at 77 K using the Brunauer–Emmett–Teller (BET) method (Micromeritics, ASAP 2020). The UV-vis diffuse reflectance spectra were recorded using a UV-vis-NIR spectrometer (Cary 5000, Varian). The valence states of Ti and O were identified by X-ray photoelectron spectroscopy (XPS), using a PHI 5000 versaprobe system using monochromatic Al KR radiation (1486.6 eV). All binding energies were referenced to the C 1s peak at 284.6 eV. The magnetic properties of the photocatalyst were evaluated at room temperature using a vibrating sample magnetometer (VSM, 9600-1 LDJ, USA) at a maximum applied field of 10 kOe.

2.4 Photocatalytic activity measurement

The photocatalytic degradation of BPA was carried out in a hollow cylindrical photoreactor. The light source is a low-pressure mercury lamp (Beijing Ceaulight Co., Model CEL-LUV254, 10 W) that emits principally near 254 nm, or a long-arc xenon lamp (Beijing Ceaulight Co., Model CEL-LAX500, 500 W) to simulate visible light (>400 nm). The photoreactor was cooled by circulating water through a quartz channel inside, and the temperature was maintained at around 25 ± 2 °C. Prior to illumination, a 300 ml suspension with a certain amount of photocatalyst (0.5 g l⁻¹) was stirred for 30 min to



ensure the homogenous dispersion and full contact of BPA (10 ppm) with catalysts. The pH of the BPA solution was controlled using a NaOH solution (5 M, 1 M, 0.1 M) and an HNO₃ solution (2 M, 0.1 M) to prepare basic and acidic solutions, respectively. After that, the lamp was turned on to irradiate the solution. A sample of 0.5 ml of solution was withdrawn at every 30 min. Moreover, the pH of the BPA solution was recorded at different reaction times using a pH meter (Mettler Toledo). The BPA concentration in each batch was measured by high-performance liquid chromatography (HPLC) equipped with a C-18 column (LUNA 5u 100A, 4.6 mm × 250 mm, Phenomenex) and a diode array detector (SPD-M20A, Shimadzu). The isocratic methanol–water mixture (70 : 30, v/v) as an eluent was employed at a flow rate of 1 ml min⁻¹. The residual BPA content in the aqueous solution was determined with a standard curve ($R^2 = 0.9999$) using a standard BPA solution for the calibration (i.e., 0, 0.2, 0.5, 1, 2, 5, 10 and 15 ppm). The degradation efficiency (DE) of BPA was calculated by the following equation: $DE = C_0/C_t$, where C_0 and C_t are the initial and residual BPA concentration (ppm) at different reaction times, respectively.

3. Results and discussion

3.1 Crystal structure, morphology and texture

The crystal structure of the hybrid was identified by XRD. As shown in Fig. 1, all the samples displayed the same

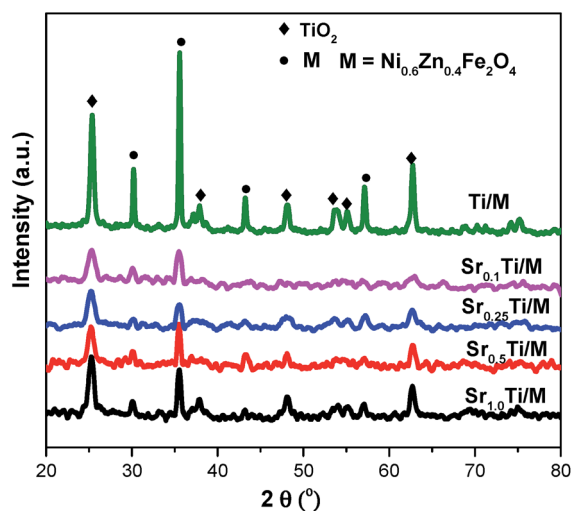


Fig. 1 XRD patterns for Sr²⁺-doped TiO₂/Ni_{0.6}Zn_{0.4}Fe₂O₄ nano-composites with a series of concentrations of Sr²⁺.

diffraction peaks, which are indexed to a mixture of the anatase phase of TiO₂ (JCPDS no. 21-1272) and the spinel phase of Ni_{0.6}Zn_{0.4}Fe₂O₄.^{43,44} No additional peaks for perovskite SrTiO₃ or SrO crystallites appeared because of the low calcination temperature and low dopant concentration of Sr²⁺.^{23,27} Noticeably, Ti/M without Sr²⁺ dopant exhibited sharp diffraction peaks. By contrast, Sr_xTi/M showed broadened and weakened diffraction peaks for both the TiO₂ (101) plane and magnetic Ni_{0.6}Zn_{0.4}Fe₂O₄. This comparison indicated that doping Sr²⁺ ions into the TiO₂ lattice could stabilize the crystal phase of TiO₂ anatase and inhibit the aggregation and growth of the particles, thus inducing a decrease in TiO₂ crystalline size. Among the samples, Sr_{0.1}Ti/M showed the smallest crystalline size (see Table 1). Increasing the concentration of Sr²⁺ ions resulted in an increase in the TiO₂ crystalline size from 15.7 nm to 18.8 nm, probably because the excessive Sr²⁺ ions cannot be completely doped into the TiO₂ lattice and caused particle agglomeration. Moreover, the uniformly dispersed Sr–TiO₂ particles may fully attach on the surface of Ni_{0.6}Zn_{0.4}Fe₂O₄ and result in a decrease in its peak intensity.

The morphology and particle size of the Sr_xTi/M samples were characterized by SEM (Fig. 2) and TEM (Fig. 3). As shown in Fig. 2, Sr_{0.1}Ti/M and Sr_{0.25}Ti/M have uniformly dispersed particles with an average size of 20 nm. By contrast, Sr_{1.0}Ti/M has randomly mixed small particles and big grains (over 100 nm). The TEM image at a low magnification in Fig. 3a further confirmed that Sr_{0.1}Ti/M was composed of relatively uniform spherical or rectangle particles with a diameter of ~20 nm. The TEM image at a high magnification in Fig. 3b clearly shows well-faceted TiO₂ nanocrystals with an interplanar spacing of 0.352 nm that matches the (101) plane of anatase phase.^{5,45,46} Ni_{0.6}Zn_{0.4}Fe₂O₄ nanoparticles (~15 nm), located beyond TiO₂ particles, was also observed with a lattice spacing of 0.187 nm.⁴⁷ Again, SEM and TEM images directly supported the XRD observations that a small amount of Sr²⁺ (below 0.25 wt%) doped TiO₂ particles were well-patched onto the magnetic Ni_{0.6}Zn_{0.4}Fe₂O₄, while excessive Sr²⁺ dopant easily induced particles aggregation into large grains.

Table 1 also compared the measured BET surface area, pore size, pore volume of the Sr_xTi/M samples to explore the effect of Sr²⁺-dopant content on the textural property. The presence of mesopores in Sr_xTi/M could result from the space between particles, as evidenced by the SEM images in Fig. 2. At low loadings of Sr²⁺, Sr_{0.1}Ti/M and Sr_{0.25}Ti/M displayed similar surface areas, pore sizes, and pore volumes, which were

Table 1 The BET surface area, pore volume, pore size, and crystallite size of TiO₂ for Sr²⁺-doped TiO₂/M (M = Ni_{0.6}Zn_{0.4}Fe₂O₄)

Sample name	BET surface area (m ² g ⁻¹)	Pore volume (cm ³ g ⁻¹)	Pore size (nm)	Crystallite size of TiO ₂ (nm)
Sr _{0.1} Ti/M	64	0.205	12.7	15.7
Sr _{0.25} Ti/M	66	0.198	12.0	15.9
Sr _{0.5} Ti/M	44	0.063	5.6	17.5
Sr _{1.0} Ti/M	46	0.071	6.1	18.8



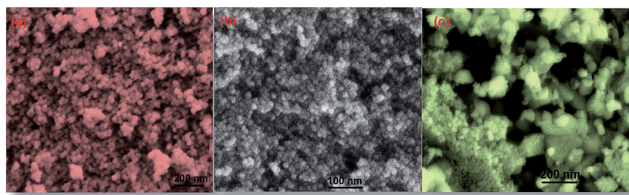


Fig. 2 SEM images for (a) $\text{Sr}_{0.1}\text{Ti}/\text{M}$, (b) $\text{Sr}_{0.25}\text{Ti}/\text{M}$, and (c) $\text{Sr}_{1.0}\text{Ti}/\text{M}$ composites ($\text{M} = \text{Ni}_{0.6}\text{Zn}_{0.4}\text{Fe}_2\text{O}_4$).

considerably higher than those of $\text{Sr}_{0.5}\text{Ti}/\text{M}$ and $\text{Sr}_{1.0}\text{Ti}/\text{M}$ at high loadings of Sr^{2+} . The data in Table 1 agrees well with XRD and SEM observations that high contents of Sr^{2+} results in the aggregation of the particles and the growth in crystalline size, which could block the micro/meso-pores within TiO_2 particles and decrease the BET surface area, pore size, and pore volume.

3.2 Optical property and chemical state

UV-vis spectra, displayed in absorbance units, have been recorded to investigate the light response of the $\text{Sr}_x\text{Ti}/\text{M}$ samples. As shown in Fig. 4, the absorption edge of bare $\text{TiO}_2(\text{P25})$ is located around 400 nm, corresponding to a band gap of about 3.10 eV. By contrast, incorporating the magnetic $\text{Ni}_{0.6}\text{Zn}_{0.4}\text{Fe}_2\text{O}_4$ with TiO_2 induced the appearance of a tail extending to a longer wavelength of 600 nm. All the $\text{Sr}_x\text{Ti}/\text{M}$ samples display similar broad bands extending to nearly 800 nm, which is consistent with the dark gray physical appearance of the samples. Furthermore, the band edge of $\text{Sr}_{0.1}\text{Ti}/\text{M}$ red shifted to about 520 nm, corresponding to a small band gap of 2.4 eV. The UV-vis results confirmed our original hypothesis that doping Sr^{2+} into TiO_2 and coupling it with magnetic $\text{Ni}_{0.6}\text{Zn}_{0.4}\text{Fe}_2\text{O}_4$ could narrow the band gap of TiO_2 and harvest visible light.

XPS has been conducted to approach the chemical states of TiO_2 with and without doping Sr. As shown in Fig. 5a, Ti/M displayed $\text{Ti } 2p_{3/2}$ and the $\text{Ti } 2p_{1/2}$ binding energies at 458.6 and 464.2 eV, respectively, corresponding to a typical characteristic of the Ti^{4+} oxidation state.^{16,40} Interestingly, the $\text{Ti } 2p$ binding energies of $\text{Sr}_{0.1}\text{Ti}/\text{M}$ slightly shifted to a lower level (by 0.4 eV). Similarly, doping Sr^{2+} into TiO_2 also led to a chemical shift in the O 1s binding energy at 529.9 eV that is

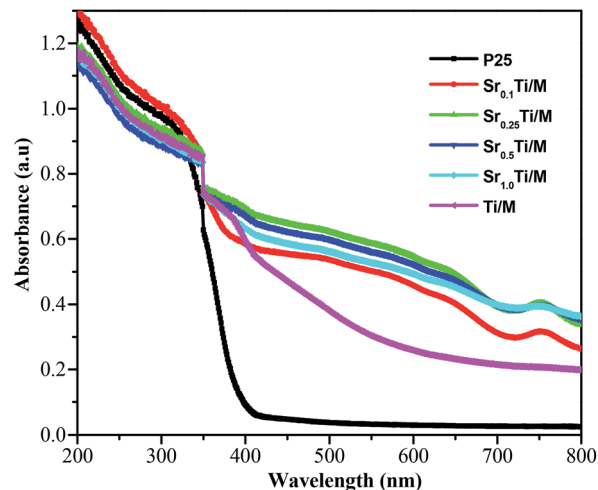


Fig. 4 UV-vis spectra for Sr^{2+} -doped $\text{TiO}_2/\text{Ni}_{0.6}\text{Zn}_{0.4}\text{Fe}_2\text{O}_4$ nano-composites with different Sr^{2+} concentrations.

associated with lattice oxygen (O_l) bonded to metal ions, while the O 1s related to surface oxygenated species (O_a) (e.g., OH groups, adsorbed H_2O) remained at a same position at 531.5 eV.⁴⁵ Moreover, the relative amount of O_l (by calculating the peak area ratio of $\text{O}_l/(\text{O}_l + \text{O}_a)$ in Fig. 5b) in $\text{Sr}_{0.01}\text{Ti}/\text{M}$ (78.6%) was slightly higher than that in Ti/M (74.8%). Generally, the chemical shifts in XPS spectra resulted from either the formation of a new oxidation state or the changes in the local chemical and physical environment. Because no shoulder peak for the new state of Ti^{3+} was observed in $\text{Sr}_{0.1}\text{Ti}/\text{M}$, the slight chemical shift is primarily related to a change in the local chemical environment of TiO_2 . In other words, Sr^{2+} has been successfully doped into TiO_2 lattice. Because some Ti^{4+} sites have been substituted by Sr^{2+} ions, some defects (e.g., oxygen vacancy, V_O) were formed for charge compensation.^{16,29} This is also supported by the XPS quantitative analysis that Ti/M has a higher ratio of $\text{O}/(\text{Ti} + \text{Zn} + \text{Ni} + \text{Fe})$ (2.61) than does $\text{Sr}_{0.1}\text{Ti}/\text{M}$ (2.02). Hence, the change in the chemical environment of TiO_2 was possibly caused by the partial replacement of Ti^{4+} by Sr^{2+} dopants and the formation of V_O in TiO_2 .

3.3 Photocatalytic performance measurement

Photocatalytic degradation of BPA over the hybrid $\text{Sr}_x\text{Ti}/\text{M}$ was first conducted under UV (254 nm) irradiation. Fig. 6 compares the photodegradation efficiency of various $\text{Sr}_x\text{Ti}/\text{M}$. Right before the photodegradation, a background experiment was carried out without UV irradiation in the presence of $\text{Sr}_{0.1}\text{Ti}/\text{M}$. The result showed that in the dark process, the concentration of BPA almost remained same as the initial one within 4 h, indicating that no photocatalytic reaction took place without photo-illumination. At low contents of Sr^{2+} , $\text{Sr}_{0.1}\text{Ti}/\text{M}$ and $\text{Sr}_{0.25}\text{Ti}/\text{M}$ exhibited similar photodegradation activity. Furthermore, increasing the concentration of Sr^{2+} resulted in a decrease in the activity over $\text{Sr}_{0.5}\text{Ti}/\text{M}$ and $\text{Sr}_{1.0}\text{Ti}/\text{M}$. By correlating the structure and property of the materials (see the results in Table 1, Fig. 1 and 2), the inferior activity at a high content of Sr^{2+} is probably

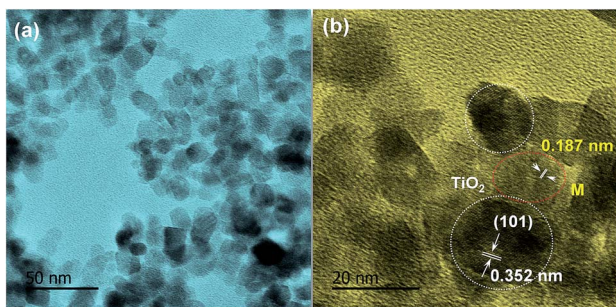


Fig. 3 (a) TEM and (b) HRTEM images for $\text{Sr}_{0.1}\text{Ti}/\text{M}$ ($\text{M} = \text{Ni}_{0.6}\text{Zn}_{0.4}\text{Fe}_2\text{O}_4$).



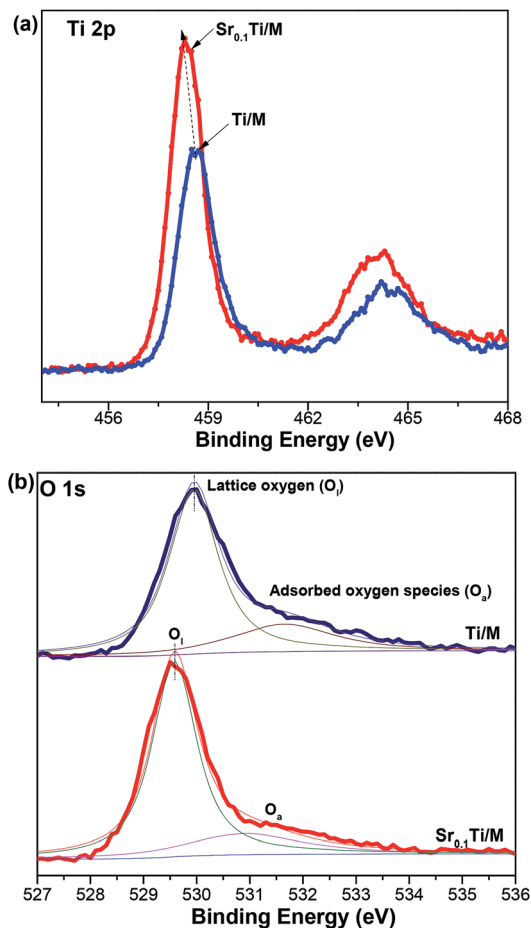


Fig. 5 XPS spectra for undoped $\text{TiO}_2/\text{Ni}_{0.6}\text{Zn}_{0.4}\text{Fe}_2\text{O}_4$ and $\text{Sr}_{0.1}\text{Ti}/\text{Ni}_{0.6}\text{Zn}_{0.4}\text{Fe}_2\text{O}_4$ composites: (a) Ti 2p, and (b) O 1s.

because $\text{Sr}_{0.5}\text{Ti}/\text{M}$ and $\text{Sr}_{1.0}\text{Ti}/\text{M}$ have larger crystalline sizes, smaller specific surface areas and pore volumes, and less uniform particle dispersions. These drawbacks on $\text{Sr}_{0.5}\text{Ti}/\text{M}$ and $\text{Sr}_{1.0}\text{Ti}/\text{M}$ could hinder the adsorption and activation of BPA on the surface. Excessive Sr^{2+} may also induce the formation of a new e^- - h^+ recombination center that shortened the lifetime of photogenerated charge carriers.²⁸ Another important result in Fig. 6 is that $\text{Sr}_{0.1}\text{Ti}/\text{M}$ and $\text{Sr}_{0.25}\text{Ti}/\text{M}$ displayed a considerably higher efficiency compared to Ti/M , $\text{Sr}_{0.25}\text{Ti}$, commercial $\text{TiO}_2(\text{P25})$, and bare M. $\text{Sr}_{0.1}\text{Ti}/\text{M}$ is able to eliminate nearly 100% BPA at 4 h, while $\text{TiO}_2(\text{P25})$ and bare M can only reach 40% and 25%, respectively. In addition, $\text{Sr}_{0.25}\text{Ti}$ and Ti/M was even more active than bare $\text{TiO}_2(\text{P25})$ and M. In this regard, it is believed that there is a synergy between Sr^{2+} dopant and magnetic M that remarkably prevents the charge recombination in TiO_2 , as a consequence of leading to a superior activity of $\text{Sr}_{0.1}\text{Ti}/\text{M}$.

We also performed photocatalytic degradation of BPA at different pH conditions using a $\text{Sr}_{0.25}\text{Ti}/\text{M}$ composite under UV irradiation because the waste water may be acidic or basic. The initial pH of the reactant solution was controlled by adding a desired amount of NaOH or HNO_3 . Fig. 7a compares the photocatalytic performance of $\text{Sr}_{0.25}\text{Ti}/\text{M}$ in a pH range of 4–10. It

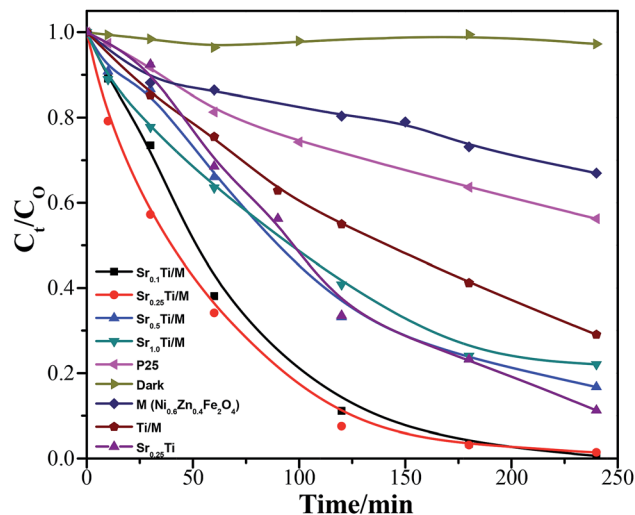


Fig. 6 Photodegradation of BPA by various Sr^{2+} -doped TiO_2/M ($\text{M} = \text{Ni}_{0.6}\text{Zn}_{0.4}\text{Fe}_2\text{O}_4$) catalysts under UV-254 nm irradiation as a function of time (catalyst dosage = 0.5 mg mL^{-1} , initial BPA concentration = 10 ppm, near neutral pH).

was found that either at basic (pH = 10) or acidic conditions (pH = 4), $\text{Sr}_{0.25}\text{Ti}/\text{M}$ displayed a higher efficiency than at near neutral conditions (pH = 6–8) within the beginning 2 h, while the efficiency eventually remained almost the same at the later stage and reached as high as nearly 99% at 3.5 h in the entire pH range (4–10). This result strongly suggested that our novel hybrid $\text{Sr}_x\text{Ti}/\text{M}$ is able to efficiently work at a wide pH range. Moreover, the pH evolution during the photocatalytic reaction was also monitored, as shown in Fig. 7b. At a basic condition, the pH gradually decreased and reached a steady state to near neutral, while at an acidic condition, the initial pH gradually increased. If starting with a near neutral solution, the pH only slowly decreased. The evolution of solution pH revealed that both proton (H^+) and OH^- radicals play a critical role in the photodegradation of BPA. A possible mechanism has been proposed to explain the pH impacts, as shown in Fig. 8. The starting solution with a high pH contains more OH^- anions, which could act as hole (h^+) scavengers and react with photogenerated h^+ to form active OH^\bullet radicals (Fig. 8a).^{16,27} Hence, the consumption of OH^- led to the decrease in pH over the reaction time. The OH^\bullet radicals have a strong oxidation ability to degrade BPA to CO_2 and H_2O , which could explain why the activity is higher at pH = 10. On the other hand, the starting solution with a low pH contains more H^+ ions, which serves as electron scavengers and inhibits the recombination of e^- - h^+ pairs (Fig. 8b). Moreover, the H^\bullet radicals, generated from $\text{H}^+ + e^- \rightarrow \text{H}^\bullet$, could react with O_2 to form hydrogen peroxide that decomposes into oxidative OH^\bullet under UV irradiation.⁴⁸ Thus, the suppressed recombination and the formation of OH^\bullet leads to an increase in pH over time and a higher efficiency than at neutral pH values.

The photocatalytic performance of the $\text{Sr}_x\text{Ti}/\text{M}$ samples was also evaluated under visible light (400–1000 nm) irradiation, as shown in Fig. 9. The order of activity of the hybrids was $\text{Sr}_{0.1}\text{Ti}/\text{M}$



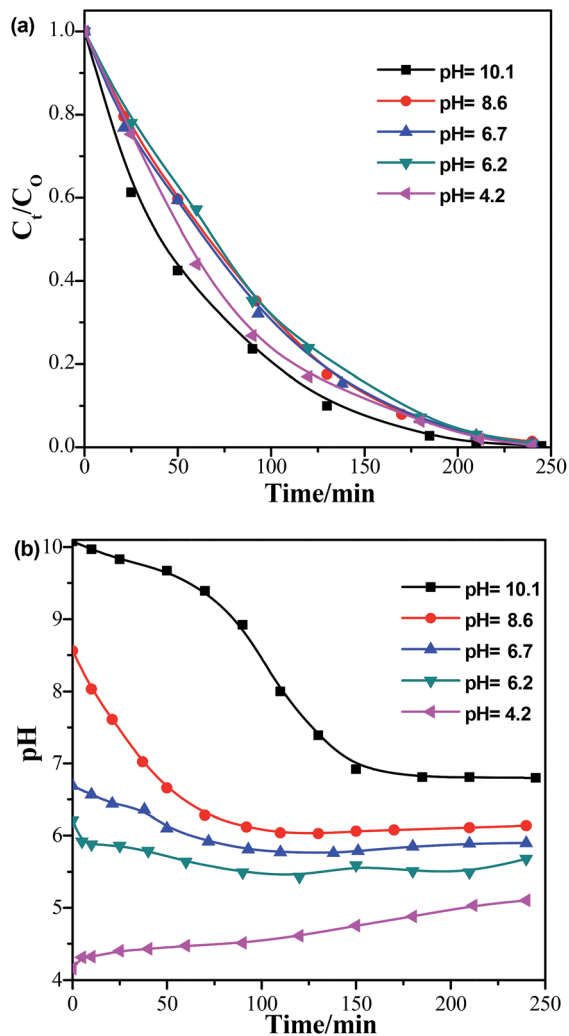


Fig. 7 Photodegradation of BPA by $\text{Sr}_{0.25}\text{Ti}/\text{M}$ ($\text{M} = \text{Ni}_{0.6}\text{Zn}_{0.4}\text{Fe}_2\text{O}_4$) under UV-254 nm irradiation (a) at different pH environments and (b) the evolution of pH as a function of time (catalyst dosage = 0.5 mg ml^{-1} , initial BPA concentration = 10 ppm).

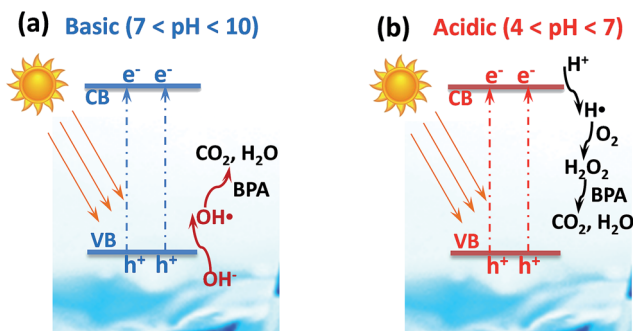


Fig. 8 The possible mechanism for BPA photodegradation under (a) basic and (b) acidic conditions.

$\text{M} > \text{Sr}_{0.25}\text{Ti}/\text{M} \approx \text{Sr}_{0.5}\text{Ti}/\text{M} \approx \text{Sr}_{1.0}\text{Ti}/\text{M} > \text{Sr}_{0.25}\text{Ti} > \text{Ti}/\text{M} > \text{P25} > \text{M}$, which is very similar to the trend under UV irradiation (see Fig. 6). Even under visible light irradiation, the photodegradation efficiency of $\text{Sr}_{0.1}\text{Ti}/\text{M}$ could reach as high as 90%

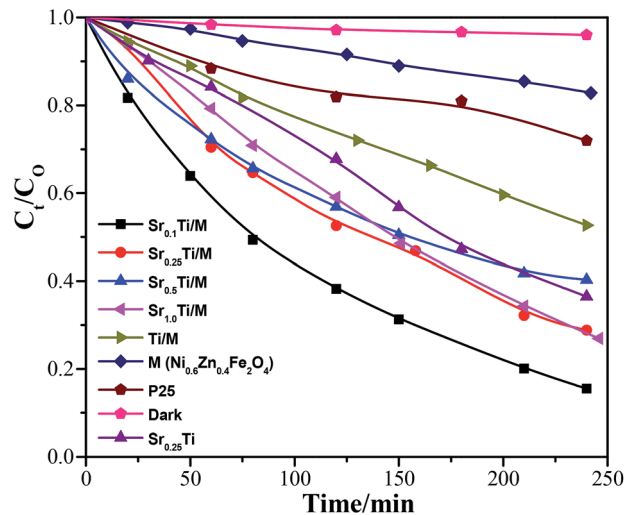


Fig. 9 Photodegradation of BPA by various Sr^{2+} -doped TiO_2/M ($\text{M} = \text{Ni}_{0.6}\text{Zn}_{0.4}\text{Fe}_2\text{O}_4$) catalysts under visible light irradiation (400–1000 nm) as a function of time (catalyst dosage = 0.5 mg ml^{-1} , initial BPA concentration = 10 ppm , near neutral pH).

at 4 h, nearly 4 times higher than bare $\text{TiO}_2(\text{P25})$ and M (only 15–20%). In addition to the larger surface area, smaller crystalline size, and more uniform particle dispersion, the superior performance of $\text{Sr}_{0.1}\text{Ti}/\text{M}$ under visible light is probably also due to another two reasons. First, incorporating an appropriate amount of Sr^{2+} dopant and magnetic M with TiO_2 narrowed its band gap (see UV-vis spectra in Fig. 4); thus, enhancing the harvest and utilization of visible light. Second, as evidenced by XPS results, doping Sr^{2+} into TiO_2 also created some active defect sites (oxygen vacancies), which may induce the formation of the new energy state located below the conduction band minimum of TiO_2 . The active defect sites could facilitate charge separation and trap electrons even under visible light.^{16,28,49} The electrons accumulated at defect sites could easily attach on O_2 molecules to produce powerful superoxide radicals ($\text{O}_2^{\cdot-}$) that promote the activation and oxidation of BPA molecules.

3.4 Material separation and cycling performance

The above photocatalytic activity results indicated that among all the tested samples, $\text{Sr}_{0.1}\text{Ti}/\text{M}$ has an outstanding performance under both UV and visible light irradiation. To further understand its superiority, we measured the cycling performance of $\text{Sr}_{0.1}\text{Ti}/\text{M}$ during three runs of photodegradation alternations. In between each cycle, the spent $\text{Sr}_{0.1}\text{Ti}/\text{M}$ was separated only by adding an external magnetic field around the solution and washed with water without any high temperature treatment or centrifugation. Above all, we measured the magnetic property of $\text{Sr}_{0.1}\text{Ti}/\text{M}$ at room temperature using vibrating magnetometer. Fig. 10 shows the magnetization (M)–magnetic field (H) loop of $\text{Sr}_{0.1}\text{Ti}/\text{M}$. It was found that $\text{Sr}_{0.1}\text{Ti}/\text{M}$ exhibited a typical soft ferrite behavior with a saturated magnetization (M_s) of 19.04 emu g^{-1} , the number of which was lower than the literature reported for pure $\text{Ni}_{0.6}\text{Zn}_{0.4}\text{Fe}_2\text{O}_4$.^{42,43} This is because our $\text{Ni}_{0.6}\text{Zn}_{0.4}\text{Fe}_2\text{O}_4$ was



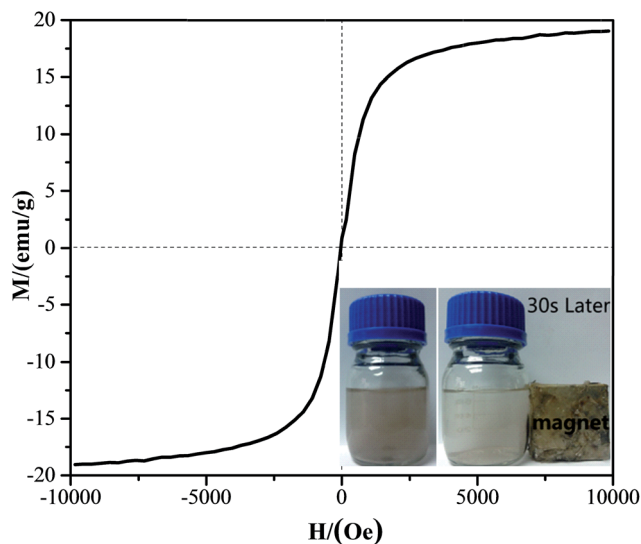


Fig. 10 Room temperature hysteresis behaviour of $\text{Sr}_{0.1}\text{Ti}/\text{M}$ ($\text{M} = \text{Ni}_{0.6}\text{Zn}_{0.4}\text{Fe}_2\text{O}_4$). Inset photograph shows a separation process of $\text{Sr}_{0.1}\text{Ti}/\text{M}$ from aqueous solution using a magnet.

encapsulated with nonmagnetic $\text{Sr}_{0.1}\text{TiO}_2$ nanoparticles. Although $\text{Sr}_{0.1}\text{Ti}/\text{M}$ has a relatively low M_s , it still can be easily magnetically separated for reuse. As evidenced by the inset photograph in Fig. 10, the suspended solution quickly became clear once placing a magnet near the bottle wall for 30 s, and the powder was accumulated and attached on the wall.

Fig. 11 compares the photodegradation efficiency of $\text{Sr}_{0.1}\text{Ti}/\text{M}$ in each cycle under both UV and visible light irradiation after 4 h. After three cycles, the efficiency in the 3rd run only slightly dropped at both conditions, but still maintained as high as 89% and 78% under UV and visible light irradiation, respectively. Obviously, $\text{Sr}_{0.1}\text{Ti}/\text{M}$ demonstrated a good stability and recyclability, where M could provide a magnetic field for

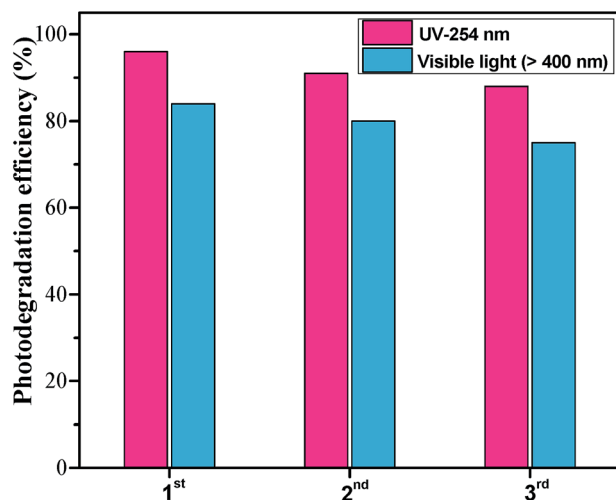


Fig. 11 The cycling performance of $\text{Sr}_{0.1}\text{Ti}/\text{M}$ ($\text{M} = \text{Ni}_{0.6}\text{Zn}_{0.4}\text{Fe}_2\text{O}_4$) for photodegradation of BPA under UV-254 nm and visible light (>400 nm) irradiation (in each cycle, BPA concentration = 10 ppm, near neutral pH).

separation and harvest visible light concurrently. This good cycling performance also confirms our original hypothesis that integrating metal ion doped photocatalysts (e.g., $\text{Sr}-\text{TiO}_2$) and magnetic materials (e.g., $\text{Ni}_{0.6}\text{Zn}_{0.4}\text{Fe}_2\text{O}_4$) is a reliable and convenient method to simultaneously enhance material separation and visible light activity for water purification.

4. Conclusions

In this work, we designed a novel hybrid photocatalyst/magnetic material, i.e., Sr^{2+} doped $\text{TiO}_2/\text{Ni}_{0.6}\text{Zn}_{0.4}\text{Fe}_2\text{O}_4$, in order to enhance the efficiency of photo-degrading organic pollutants under visible light and to easily separate and reuse the material. The hybrid was synthesized by a simple sol-gel method. We found that doping a low concentration of Sr^{2+} (below 0.25 wt%) induced a smaller crystalline size, larger surface area and pore volume, and more uniform particle dispersion than did loading a high concentration of Sr^{2+} . Moreover, doping Sr^{2+} ions and coupling a magnetic material with TiO_2 narrowed the band gap and induced the generation of defect sites in TiO_2 . As a result, the integrated hybrid with a low loading of Sr^{2+} not only demonstrated a high efficiency (over 90%) and a good recycling performance (90% maintenance) under both UV and visible light irradiation, but also can efficiently work at a wide pH range (4–10) and be easily separated only by adding an external magnetic field. Furthermore, the hybrid $\text{Sr}-\text{TiO}_2/\text{Ni}_{0.6}\text{Zn}_{0.4}\text{Fe}_2\text{O}_4$ showed an over two-times higher activity than those of $\text{TiO}_2/\text{Ni}_{0.6}\text{Zn}_{0.4}\text{Fe}_2\text{O}_4$, commercial $\text{TiO}_2(\text{P}25)$ and bare $\text{Ni}_{0.6}\text{Zn}_{0.4}\text{Fe}_2\text{O}_4$, as well as 50% higher activity than that of Sr -doped TiO_2 , indicating that there is a synergy between the doped photocatalyst and magnetic material. The findings in this work suggest a new direction to engineer a smart photocatalyst/magnetic material heterojunction and control the interface between them, and it sheds light on the material's application in other aqueous-solid phase photocatalytic reactions.

Acknowledgements

This work was financially supported by National Natural Science Foundation of China (no. 51468043), Natural Science Foundation of Jiangxi Province (no. 20132BAB203018), Jiangxi Province Youth Scientists Cultivating Object Program (no. 20112BCB23017), Key Laboratory of Photochemical Conversion and Optoelectronic Materials, TIPC, CSA (no. PCOM201401).

Notes and references

- 1 S. Y. Lee and S. J. Park, *J. Ind. Eng. Chem.*, 2013, **19**, 1761–1769.
- 2 M. A. Patil and P. A. Parikh, *Bull. Environ. Contam. Toxicol.*, 2014, **92**, 109–114.
- 3 M. N. Chong, B. Jin, C. W. Chow and C. Saint, *Water Res.*, 2010, **44**, 2997–3027.
- 4 C. Sriwong, S. Wongnawa and O. Patarapaiboolchai, *J. Environ. Sci.*, 2012, **24**, 464–472.



- 5 Z. Cheng, X. Quan, J. Xiang, Y. Huang and Y. Xu, *J. Environ. Sci.*, 2012, **24**, 1317–1326.
- 6 S. Lakshmi, R. Renganathan and S. Fujita, *J. Photochem. Photobiol., A*, 1995, **88**, 163–167.
- 7 Y. Ohko, I. Ando, C. Niwa, T. Tatsuma, T. Yamamura, T. Nakashima, Y. Kubota and A. Fujishima, *Environ. Sci. Technol.*, 2001, **35**, 2365–2368.
- 8 E. Grabowska, J. Reszczynska and A. Zaleska, *Water Res.*, 2012, **46**, 5453–5471.
- 9 M. D'Arienzo, R. Scotti, L. Wahba, C. Battocchio, E. Bemporad, A. Nale and F. Morazzoni, *Appl. Catal., B*, 2009, **93**, 149–155.
- 10 P. Tian, H. Zhang, Z. Y. Shi, M. Y. Zhang, L. Wei and Z. Q. Yang, *Applications of Engineering Materials, Pts 1–4*, 2011, vol. 287–290, pp. 1815–1818.
- 11 V. M. Daskalaki, Z. Frontistis, D. Mantzavinos and A. Katsaounis, *Catal. Today*, 2011, **161**, 110–114.
- 12 Z. Magdolenova, A. Collins, A. Kumar, A. Dhawan, V. Stone and M. Dusinska, *Nanotoxicology*, 2014, **8**, 233–278.
- 13 S. C. Xu, Y. X. Zhang, S. S. Pan, H. L. Ding and G. H. Li, *J. Hazard. Mater.*, 2011, **196**, 29–35.
- 14 R. F. Yuan, B. H. Zhou, D. Hua and C. H. Shi, *J. Hazard. Mater.*, 2013, **262**, 527–538.
- 15 S. D. Kim, W. G. Choe and J. R. Jeong, *Ultrason. Sonochem.*, 2013, **20**, 1456–1462.
- 16 B. F. Gao, T. M. Lim, D. P. Subagio and T. T. Lim, *Appl. Catal., A*, 2010, **375**, 107–115.
- 17 X. P. Wang, Y. X. Tang, M. Y. Leiw and T. T. Lim, *Appl. Catal., A*, 2011, **409**, 257–266.
- 18 R. H. Zhang, Q. Wang, J. Liang, Q. Li, J. F. Dai and W. X. Li, *Phys. B*, 2012, **407**, 2709–2715.
- 19 D. Avisar, I. Horovitz, L. Lozzi, F. Ruggieri, M. Baker, M. L. Abel and H. Mamane, *J. Hazard. Mater.*, 2013, **244**, 463–471.
- 20 C. H. Wu, C. Y. Kuo, C. J. Lin and P. K. Chiu, *Int. J. Photoenergy*, 2013, **2013**, 1–9.
- 21 L. G. Devi and R. Kavitha, *Appl. Catal., B*, 2013, **140**, 559–587.
- 22 H. R. Rajabi, O. Khani, M. Shamsipur and V. Vatanpour, *J. Hazard. Mater.*, 2013, **250**, 370–378.
- 23 I. R. Qazi, W.-J. Lee, H.-C. Lee, M. S. Hassan and O. B. Yang, *J. Nanosci. Nanotechnol.*, 2010, **10**, 3430–3434.
- 24 F. Zou, Z. Jiang, X. Qin, Y. Zhao, L. Jiang, J. Zhi, T. Xiao and P. P. Edwards, *Chem. Commun.*, 2012, **48**, 8514–8516.
- 25 O. Ruzimuradov, S. Nurmanov, M. Hojamberdiev, R. M. Prasad, A. Gurlo, J. Broetz, K. Nakanishi and R. Riedel, *Mater. Lett.*, 2014, **116**, 353–355.
- 26 Y. Zhang, S. Lin, W. Zhang, H. Ge, G. Li, Y. Zhang, F.-Y. Qi and X.-M. Song, *RCS Adv.*, 2014, **4**, 3226–3232.
- 27 L. Kumaresan, M. Mahalakshmi, M. Palanichamy and V. Murugesan, *Ind. Eng. Chem. Res.*, 2010, **49**, 1480–1485.
- 28 D. Li, J.-F. Huang, L.-Y. Cao, J.-Y. Li, H.-B. OuYang and C.-Y. Yao, *Ceram. Int.*, 2014, **40**, 2647–2653.
- 29 A. Zacharakis, E. Chatzisyseon, V. Binas, Z. Frontistis, D. Venieri and D. Mantzavinos, *Int. J. Photoenergy*, 2013, **2013**, 1–9.
- 30 N. Miranda-Garcia, S. Suarez, M. I. Maldonado, S. Malato and B. Sanchez, *Catal. Today*, 2014, **230**, 27–34.
- 31 J. Hou, G. Dong, Y. Ye and V. Chen, *J. Membr. Sci.*, 2014, **469**, 19–30.
- 32 C.-Y. Kuo, C.-H. Wu and H.-Y. Lin, *Environ. Technol.*, 2014, **35**, 1851–1857.
- 33 E. M. Saggioro, A. S. Oliveira, T. Pavesi, M. Jimenez Tototzintle, M. Ignacio Maldonado, F. V. Correia and J. C. Moreira, *Environ. Sci. Pollut. Res.*, 2014, **21**, 12112–12121.
- 34 S. Xu, W. Shangguan, J. Yuan, M. Chen and J. Shi, *Appl. Catal., B*, 2007, **71**, 177–184.
- 35 P. M. Álvarez, J. Jaramillo, F. López-Piñero and P. K. Plucinski, *Appl. Catal., B*, 2010, **100**, 338–345.
- 36 D. F. Sun, Y. D. Han, S. Gao and X. L. Zhang, *Surf. Coat. Technol.*, 2013, **228**, S516–S519.
- 37 M. Feyzi, H. R. Rafiee, S. Ranjbar, F. Jafari and B. Safari, *Mater. Res. Bull.*, 2013, **48**, 4844–4849.
- 38 Y. H. Tang, G. Zhang, C. B. Liu, S. L. Luo, X. L. Xu, L. Chen and B. G. Wang, *J. Hazard. Mater.*, 2013, **252**, 115–122.
- 39 X. X. Yu, S. W. Liu and J. G. Yu, *Appl. Catal., B*, 2011, **104**, 12–20.
- 40 A. Abd Aziz, K. S. Yong, S. Ibrahim and S. Pichiah, *J. Hazard. Mater.*, 2012, **199**, 143–150.
- 41 K. Praveena, K. Sadhana, S. Srinath and S. R. Murthy, *J. Phys. Chem. Solids*, 2013, **74**, 1329–1335.
- 42 Z. Wang, Y. Xie, P. Wang, Y. Ma, S. Jin and X. Liu, *J. Magn. Magn. Mater.*, 2011, **323**, 3121–3125.
- 43 V. D. Kapse, S. A. Ghosh, F. C. Raghuvanshi and S. D. Kapse, *Mater. Chem. Phys.*, 2009, **113**, 638–644.
- 44 T. Slatineanu, A. R. Iordan, M. N. Palamaru, O. F. Caltun, V. Gafton and L. Leontie, *Mater. Res. Bull.*, 2011, **46**, 1455–1460.
- 45 J. W. Ng, X. P. Wang and D. D. Sun, *Appl. Catal., B*, 2011, **110**, 260–272.
- 46 L. Liu, D. T. Pitts, H. Zhao, C. Zhao and Y. Li, *Appl. Catal., A*, 2013, **467**, 474–482.
- 47 B. Xu, B. Huang, H. Cheng, Z. Wang, X. Qin, X. Zhang and Y. Dai, *Chem. Commun.*, 2012, **48**, 6529–6531.
- 48 C. G. Park, E. S. Choi, H. W. Jeon, J. H. Lee, B. W. Sung, Y. H. Cho and K. B. Ko, *Desalin. Water Treat.*, 2014, **52**, 797–804.
- 49 S. Ghasemi, S. Rahimnejad, S. R. Setayesh, S. Rohani and M. R. Gholami, *J. Hazard. Mater.*, 2009, **172**, 1573–1578.

